

Non-equilibrium plasma activated durable molybdenum oxycarbide electrocatalysts for acidic hydrogen evolution up to 10 A cm^{-2}

Received: 3 March 2025

Accepted: 22 October 2025

Published online: 28 November 2025

 Check for updates

Shiwen Wu  ^{1,5}, Taesoon Hwang  ^{2,5}, Amirarsalan Mashhadian ^{1,5}, Tianyi Li  ³, Yuzi Liu  ⁴, Dewen Hou ⁴✉, Kyeongjae Cho  ²✉ & Guoping Xiong  ¹✉

Electrocatalytic hydrogen evolution in acidic media at industrial-level current densities is limited by high overpotential, performance degradation, and consequently low throughput. To address these challenges, we develop nanoedge-enriched molybdenum oxycarbide (MoO_xC_y) electrocatalysts with a uniform phase by non-equilibrium plasma-enhanced chemical vapor deposition. The vertically standing MoO_xC_y exhibits a low overpotential of 415 mV and stable long-term operation (~ 0.11% performance degradation over 1000 h) at high current densities up to 10 A cm^{-2} , corresponding to a high hydrogen throughput of $4,477.4 \text{ L cm}^{-2}$, which exceeds the Department of Energy targets. Molybdenum oxycarbide catalysts are competitive with state-of-the-art transition-metal and even noble-metal catalysts in terms of throughput and lifetime throughput. The key mechanism involves carbon incorporation into MoO_2 lattices, which lowers the Mo valence and weakens Mo-H binding energy, thereby improving hydrogen evolution performance. Density functional theory results suggest that carbon atoms in MoO_xC_y increase the binding energy between Mo and the adjacent atoms, enhancing MoO_xC_y structural stability. This study establishes a pathway toward practical and efficient transition-metal catalysts for hydrogen evolution.

Electrochemical water splitting in acidic media offers a cost-effective and promising approach for producing clean hydrogen with high purity through the hydrogen evolution reaction (HER)^{1–3}. For practical industrial applications, it is essential to develop electrocatalysts that can maintain low overpotentials (ensuring high energy conversion efficiency from electricity to hydrogen chemical energy) and extend operating durations (to minimize the catalyst replacement frequency) with high hydrogen throughput at ultrahigh current densities (enabling higher volume hydrogen production at a given facility size). Many critical factors, such as the oxygen evolution reaction (OER) at anode catalysts, the durability of the proton exchange membrane, and the HER at cathode catalysts, affect the

efficiency and long-term reliability of practical water-splitting systems. These challenges become even more severe at industrial-level high current densities ($>3 \text{ A cm}^{-2}$). Among these, cathode materials, including the best noble metal-based catalysts, often suffer from poor stability, sluggish kinetics, and mass transport limitations under such demanding conditions. For instance, noble metal-based electrocatalysts, despite their excellent performance at low current densities, still suffer from poor long-term stability⁴, high overpotential^{5,6}, and costly synthesis⁷, resulting in overall industrial-level HER performance that falls short of the U.S. Department of Energy (DOE) target (i.e., $>3 \text{ A cm}^{-2}$ for 1000 h with 0.13% performance degradation)⁸. Transition metal-based electrocatalysts (e.g.,

¹Department of Mechanical Engineering, The University of Texas at Dallas, Richardson, TX, USA. ²Department of Material Science Engineering, The University of Texas at Dallas, Richardson, TX, USA. ³X-ray Science Division, Argonne National Laboratory, Lemont, IL, USA. ⁴Center for Nanoscale Materials, Argonne National Laboratory, Lemont, IL, USA. ⁵These authors contributed equally: Shiwen Wu, Taesoon Hwang, Amirarsalan Mashhadian. ✉e-mail: houd@anl.gov; kjcho@utdallas.edu; guoping.xiong@utdallas.edu

sulfides⁹, oxides^{10,11}, and carbides^{12,13} have emerged as promising alternatives to noble metal-based catalysts for acidic HER.

Among them, transition metal carbides have attracted particular attention because of their excellent electrical conductivity and promising electrocatalytic activity toward hydrogen evolution, stemming from their analogous *d*-band electronic structure to platinum¹⁴ and consequent optimal metal-H binding energy¹⁵. However, such carbide catalysts face severe performance degradation and thus exhibit unstable operation lifetime, particularly at high current densities, because of surface oxidation^{16–18}. On the other hand, transition metal oxide catalysts such as MoO₂, albeit with excellent chemical stability and long lifetime, generally suffer from a large bandgap and low electrical conductivity, leading to sluggish charge transfer and thus inferior HER performance¹⁹. Theoretical studies have indicated that incorporating carbon into the lattices of transition metal oxides can effectively reduce their band gaps, thereby enhancing their electrical conductivity²⁰. In addition, designing catalysts with low oxygen vacancies and stabilized atomic bonding structures can improve corrosion resistance, chemical stability, and lifetime^{21,22}. Moreover, metastable materials can form a kinetically stable²³ phase, such as metastable β -NiMoO₄, which has been reported as an efficient HER catalyst with notable stability²⁴. Taken together, controllable insertion of carbon into the lattice structures of transition metal oxides to form metastable intermediates (i.e., transition metal oxycarbides) with a uniform phase and active metal-oxygen-carbon bonds seems quite promising to strike a balance between the electrocatalytic properties and chemical stability of catalysts operating under harsh conditions²⁵.

Although molybdenum carbides functionalized by oxygen surface terminations or surface-oxidized transition metal carbides are well-reported^{26,27}, incorporating carbon directly into the lattice of molybdenum oxides to synthesize metastable molybdenum oxycarbides with a uniform phase is rather challenging due to the thermodynamic tendency for phase separation into stable oxide or carbide phases²⁵. To overcome the synthesis challenges of oxycarbides, Sun et al.²⁵ recently utilized flame spray pyrolysis at 2200 °C with an iridium promoter to synthesize unsaturated Mo₁₇O₄₇, which was subsequently in-situ carburized at 600 °C for up to 100 h to form α -MoC/MoO_xC_y mixtures for efficient reverse water-gas shift applications. Equilibrium methods to synthesize MoO_xC_y require a long time and high temperature, which often leads to phase separation, grain growth, and non-uniform carbon incorporation, due to the tendency of the system to favor thermodynamically stable separated phases (e.g., pure oxides or carbides)

over metastable oxycarbides²⁶. Non-equilibrium plasmas, which are distinguished by highly energetic reactive species in a far-from-equilibrium state and their ability to work at low temperatures, provide substantial benefits over conventional approaches for the synthesis and manufacturing of novel materials^{28–30}. By operating under far-from-equilibrium conditions, non-equilibrium plasma synthesis enables atomic-level carbon incorporation at reduced processing temperatures by unique plasma-matter interactions, enhancing the reactivity of surfaces exposed to plasma species. The interactions with plasma can significantly alter the nucleation and crystal growth processes involved in catalyst preparation, facilitating thermodynamically unfavorable reactions that are not possible through conventional thermal methods^{31,32}. The plasma manufacturing method is well known to enable the synthesis of metastable phases such as diamond³³, β -tungsten³⁴, and silicon oxycarbide³⁵. With the assistance of energetic plasma species (e.g., ions, radicals), the carbon diffusion into transition metal oxides is expected to be significantly facilitated, even at low temperatures. This makes plasma-enabled nonequilibrium synthesis quite promising to generate metastable transition metal oxycarbides with controllable chemical composition, uniformly mixed phases, and structures favorable for high-performance HER³⁶.

In this work, we report an in-situ growth of vertically standing nanoedge-enriched transition metal oxycarbide (i.e., molybdenum oxycarbide, MoO_xC_y) nanosheet catalysts via plasma-enhanced chemical vapor deposition (PECVD) using earth-abundant salts (i.e., MoO₃ and NaCl) as precursors. As shown in Fig. 1, the nanoedge-enriched MoO_xC_y catalysts fabricated through non-equilibrium plasma offer the following benefits toward HER: (1) Improved long-term stability and efficiency of catalysts because of the oxycarbide phases enabled by non-equilibrium plasma, which are thermodynamically unfavorable to obtain through conventional equilibrium thermal methods; (2) Efficient hydrogen bubble detachment from the nanoedge-enriched structure with high roughness, maintaining continuous exposure of catalytic sites to the surrounding electrolyte. (3) Lowered *d*-band center of the MoO_xC_y because of the controlled introduction of carbon atoms into the lattice of MoO₂, leading to reduced Mo-H binding energy and thus improved HER. As such, the MoO_xC_y exhibits efficient acidic HER performance with a low overpotential (η) of 415 mV at a high current density (j) of up to 10 A cm⁻² for 1000 h with negligible degradation (approx. 0.11%), corresponding to a high hydrogen (H₂) throughput of over 4477.4 L cm⁻² and expected lifetime of 90,909 h, surpassing the DOE goal (>1253.7 L cm⁻² and 80,000 h with <10%

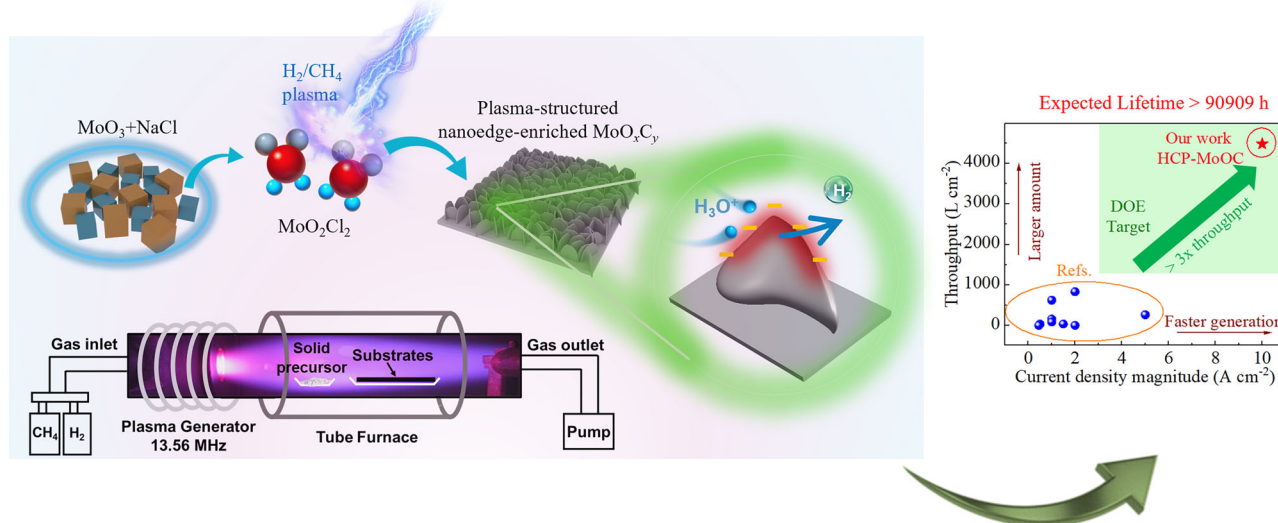


Fig. 1 | Schematic illustration of the synthesis of MoO_xC_y electrocatalysts. The PECVD-grown MoO_xC_y nanosheets serve as a catalyst with enhanced efficiency and durability toward electrocatalytic hydrogen evolution.

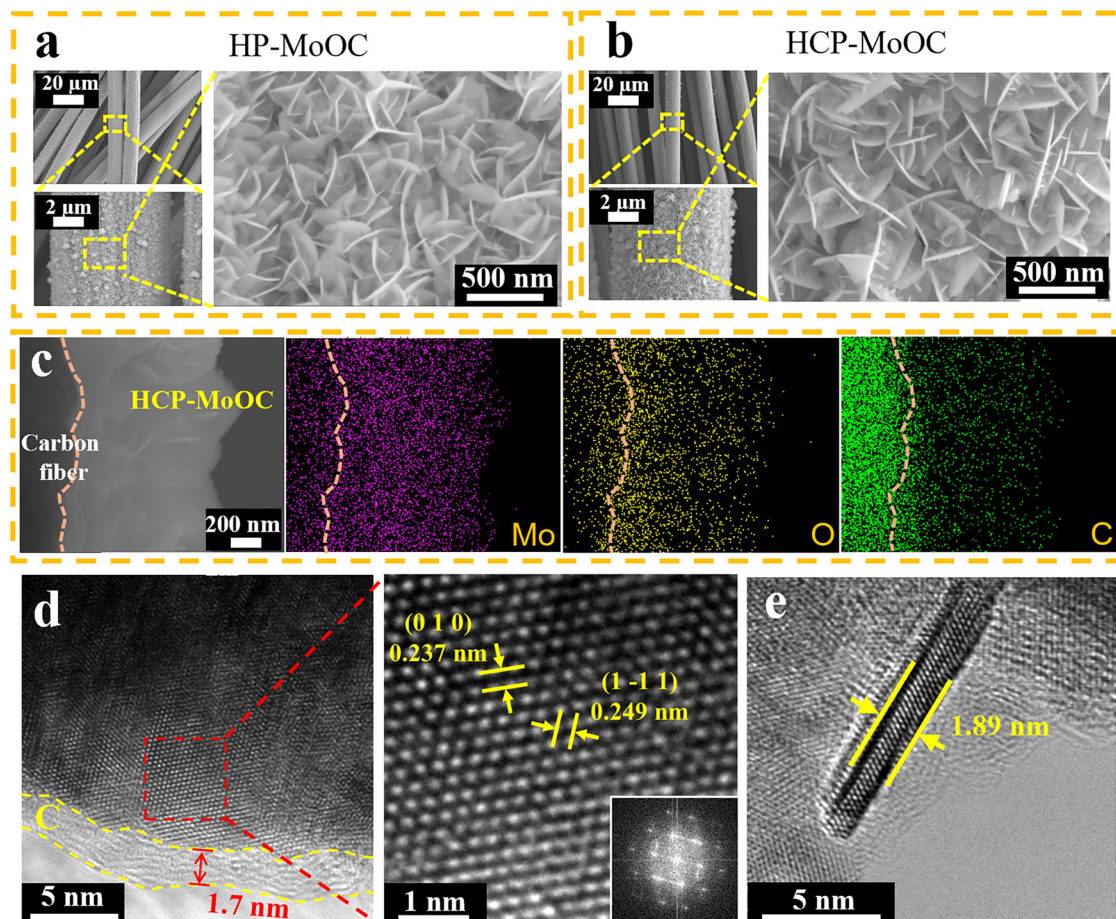


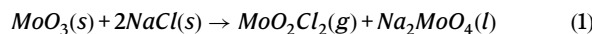
Fig. 2 | Structural characterization of MoO_xC_y . SEM images of **a** HP-MoOC and **b** HCP-MoOC. **c** Cross-sectional SEM image and elemental mappings of the HCP-MoOC. **d** HRTEM image of HCP-MoOC with the corresponding FFT pattern in the inset. **e** HRTEM image showing the thickness of a single MoO_xC_y nanosheet within HCP-MoOC.

degradation⁸ and demonstrating competitiveness with state-of-the-art transition metal- and even noble metal-based catalysts. This work sheds light on the underlying mechanism of developing high-throughput transition metal oxycarbide catalysts for practical industrial applications in electrocatalytic acidic hydrogen evolution.

Results

Synthesis and characterization of the MoO_xC_y catalyst

Vertically standing, nanoedge-enriched MoO_2 samples (denoted as HP-MoO₂) were fabricated using PECVD on nickel foam (Supplementary Fig. S1). The MoO_2 arrays were synthesized through a PECVD process with a salt mixture of earth-abundant MoO_3 and NaCl as the solid precursors in a non-equilibrium hydrogen plasma (HP) environment for 20 min (see details in Methods). During growth, the mixture of MoO_3 and NaCl powders was introduced into the upstream of substrates inside the tube to generate volatile metal oxychlorides (i.e., MoO_2Cl_2) at elevated temperatures as the metal precursor^{37–39}.



The gaseous MoO_2Cl_2 was subsequently guided to the nickel foam substrate, promoting the growth of MoO_2 within the highly reductive HP environment. The presence of a strong electric field in the plasma sheath can guide the growth of materials in a vertical orientation to the substrate (see Fig. S2)⁴⁰. To incorporate the carbon element into the lattice of MoO_2 and form vertically standing, nanoedge-enriched metastable MoO_xC_y (denoted HP-MoOC) arrays, the

substrate was changed to carbon cloth. During the growth, the surface of the carbon fiber substrate was etched by HP, generating hydrocarbon species^{41,42} that served as the carbon source for MoO_xC_y formation. As shown in Fig. 2a, the PECVD-grown HP-MoOC exhibited petal-like nanosheet structures that are aligned roughly perpendicularly to the substrate. These nanostructures showed high aspect ratios and abundant exposed ultrasharp nanoedges. This morphology is distinctly different from the particle-like or horizontally stacked forms of transition metal oxides produced by conventional thermal chemical vapor deposition, as reported in previous studies^{37,38,43}. The chemical composition of HP-MoOC was determined by using energy-dispersive X-ray (EDX) spectroscopy, revealing a Mo:O:C atomic ratio of approx. 1:1.5:0.5 (Supplementary Fig. S3).

To achieve a tunable carbon content in HP-MoOC, the carbon source was further increased through additional methane plasma treatment during PECVD (see details in Methods). The resulting product, denoted as HCP-MoOC, still maintained the vertical-standing, nanoedge-enriched morphology (Fig. 2b), according to the cross-sectional scanning electron microscope (SEM) image (Fig. 2c). The vertical-standing, nanoedge-enriched morphology of HP-MoOC and HCP-MoOC is uniform throughout the substrate (Figs. S4 and S5). Elemental mapping obtained by EDX confirms the successful incorporation of carbon into the MoO_2 structure (Fig. 2c), while additional SEM and EDX analyses further demonstrate the even distribution of Mo and O elements across the sample surface (Fig. S5a and S5b), indicating homogeneous material formation. To further evaluate the spatial distribution in both HCP-MoOC and HCP-MoOC, line-scan EDX

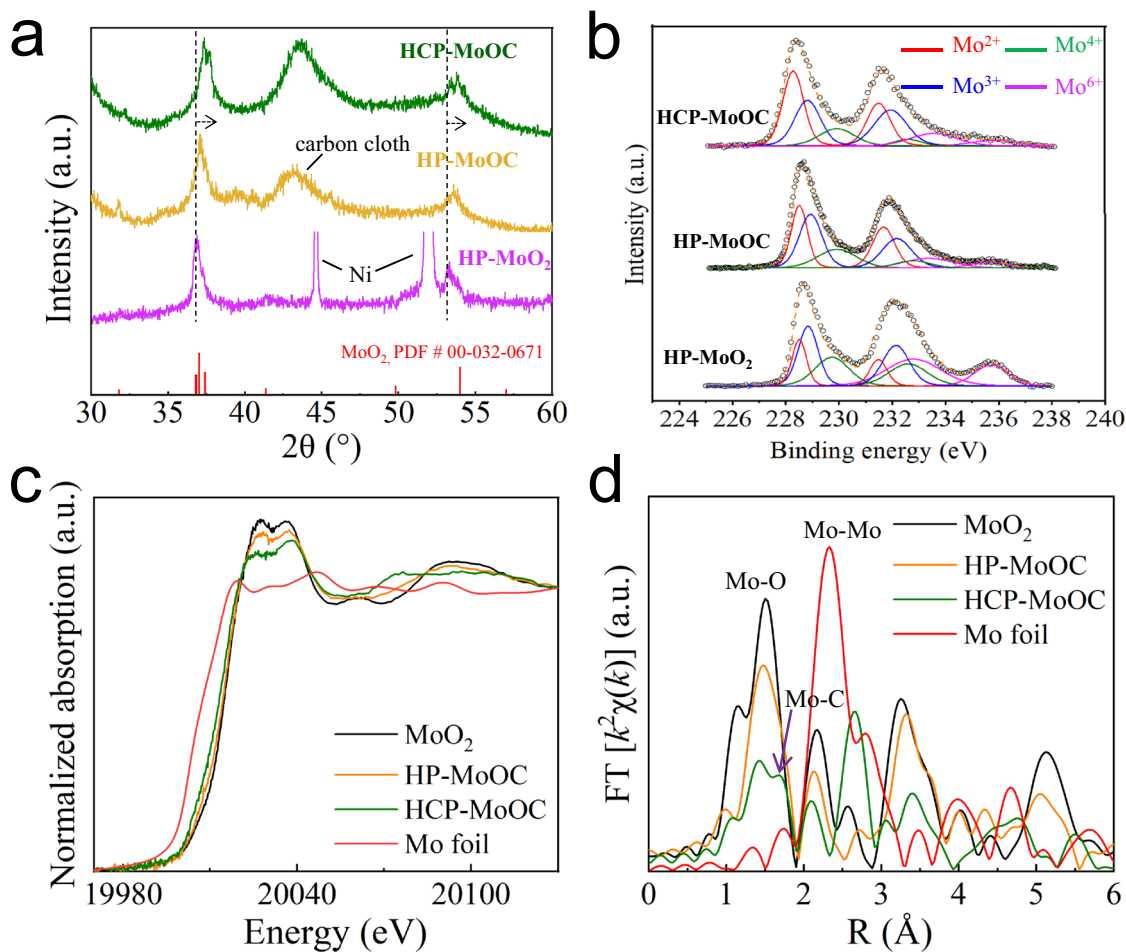


Fig. 3 | Revealing the incorporation of carbon into the MoO₂ lattices. a XRD spectra of HCP-MoOC, HP-MoOC, and HP-MoO₂. **b** Mo 3d XPS spectra of HP-MoO₂, HP-MoOC, and HCP-MoOC. **c** Mo K-edge XANES spectra of Mo-based and reference

samples. **d** Mo K-edge Fourier transform EXAFS spectra of HP-MoOC, HCP-MoOC, and reference samples.

analyses (Figs. S6 and S7) were performed along the vertical axis of representative petal structures. The results revealed a carbon concentration gradient in HP-MoOC, with higher intensity near the substrate interface. In contrast, HCP-MoOC exhibited a more uniform carbon distribution throughout the structure, attributed to the dual carbon incorporation from both the carbon cloth substrate and the CH₄ plasma treatment. However, the presence of Mo and O signals near the substrate in Fig. 2c can be attributed to the diffusion of these species into the substrate during plasma-assisted growth, a phenomenon that has also been reported in previous studies^{44,45}.

The atomic structures of the PECVD-grown MoO_xC_y electrocatalysts were evaluated by high-resolution transmission electron microscopy (HRTEM) and fast Fourier transform analyses (Fig. 2d and Supplementary Fig. S8). The TEM result reveals atomic interlayer distances of 0.237 and 0.249 nm, corresponding to the (0 1 0) and (1 -1 1) planes, respectively, of the monoclinic crystalline structure observed in both HP-MoOC and HCP-MoOC. Notably, compared to HP-MoOC (Supplementary Fig. S8), HCP-MoOC exhibited a carbon-encapsulated crystalline structure, where the crystalline MoO_xC_y was covered by a thin layer of carbon with a thickness of ~1.7 nm, as shown in Fig. 2d. This thin carbon layer influences the interlayer spacing of the first few atomic layers (up to 5 layers, as shown in Fig. S9), likely due to interfacial strain effects or increased carbon incorporation near the interface. Additionally, the lattice spacings in HCP-MoOC were different

from those in HP-MoOC, suggesting a higher degree of carbon atom incorporation into the crystalline structure of MoO₂ during the methane plasma treatment, which also leads to the formation of additional carbon layers. The TEM images captured from different regions of the HCP-MoOC sample show that the carbon layer exhibits a typical thinness of a few nanometers (Fig. S10). The presence of this carbon layer was also confirmed by Raman spectroscopy. As shown in Supplementary Fig. S11, HCP-MoOC exhibited distinct D-band ($\omega_D \sim 1350$ cm⁻¹) and G-band ($\omega_G \sim 1584$ cm⁻¹) peaks, indicating the formation of a carbon structure⁴⁶. In contrast, these peaks were absent in HP-MoOC, implying that the carbon layer forms only during the methane plasma treatment. EDX element analysis was further conducted on an individual MoO_xC_y nanosheet within the HCP-MoOC sample (Supplementary Fig. S12). Although a high carbon ratio was detected, we note that this result did not accurately reflect the true atomic ratio within the crystalline structure of HCP-MoOC due to the presence of a carbon coating layer. Additionally, the HCP-MoOC nanosheets synthesized via PECVD exhibited a thickness of only a few nanometers (Fig. 2e), while their height reached several hundred nanometers (Fig. 2c). This morphology resulted in a high aspect ratio, providing numerous active edge sites for high-performance catalytic applications.

X-ray diffraction (XRD) patterns of the PECVD-grown catalysts further confirmed the incorporation of carbon into the lattice structure of HP-MoOC (Fig. 3a). The peak of HP-MoO₂ at $2\theta = \sim 36.9^\circ$,

which corresponded to the monoclinic crystalline MoO_2 (PDF Card No. 00-032-0671)⁴⁷, showed a gradual shift toward larger values of 37.1° and 37.3° for HP-MoOC and HCP-MoOC, respectively. A similar peak shift is also observed around 55° , which can be attributed to the reduced lattice spacing caused by the incorporation of carbon atoms into the MoO_2 structure. In addition, no characteristic peaks of molybdenum carbides were observed, indicating that no phase separation occurred in the HCP-MoOC during the plasma synthesis process and confirming the formation of metastable $\text{MoO}_{x,\text{C}_y}$ with a uniform phase. This substitutional incorporation of carbon into the MoO_2 results in lattice contraction and the corresponding peak shift to higher angles. However, the preservation of the peak shape and the absence of new reflections also suggest that the original monoclinic lattice is maintained, supporting the formation of a single-phase $\text{MoO}_{x,\text{C}_y}$. The higher intensity of the carbon-related peak in HCP-MoOC ($2\theta = \sim 43.5^\circ$) is attributed to the contribution of both the carbon cloth substrate and an additional thin carbon layer on the catalyst surface.

X-ray photoelectron spectroscopy (XPS) was employed to analyze the metal valence states and electronic structures of HP-MoOC and HCP-MoOC catalysts. As displayed in Fig. 3b, the Mo 3d spectra for both HCP-MoOC, HP-MoOC, and HP-MoO₂ were decomposed into $3d_{5/2}$ and $3d_{3/2}$ peaks because of the spin-orbital coupling feature⁴⁸. For all of the catalysts, four valence states of Mo (Mo^{2+} , Mo^{3+} , Mo^{4+} , and Mo^{6+}) were observed. The presence of Mo^{4+} is consistent with the characteristic oxidation state of MoO_2 , while the emergence of Mo^{2+} and Mo^{3+} peaks suggests partial reduction of Mo, likely due to carbon incorporation into the MoO_2 lattice or the formation of oxygen vacancies in the highly reducing plasma environment. The Mo^{2+} peak in HCP-MoOC is shifted to a lower binding energy compared to that in HP-MoOC and HP-MoO₂, as shown in Fig. 3b. This shift indicates a reduced electron density around Mo atoms in HCP-MoOC, likely due to greater carbon incorporation and the difference in electronegativity between oxygen and carbon, which alters the local chemical environment. The Mo^{4+} peak area is highest in HP-MoO₂, followed by HP-MoOC and then HCP-MoOC, indicating that increased carbon incorporation leads to a progressive reduction of molybdenum to lower oxidation states. Notably, the atomic percentage of Mo^{2+} in HCP-MoOC (39.77%) was higher than that in HP-MoOC (29.24%), indicating a greater degree of chemical bonding between carbon atoms and Mo in HCP-MoOC. While the detection of Mo^{6+} in the HCP-MoOC is possible because of the surface sensitivity of XPS (~ 5 – 10 nm probing depth)⁴⁹ and the presence of a sub-2 nm-thick carbon layer that enable detection of sub-surface Mo oxidation states, the peaks at 232.2 and 235.9 eV are characteristics of Mo^{6+} and likely arises from the mild surface oxidation of the Mo-based materials when exposed to air^{50,51}.

To further elucidate the local coordination structure of the PECVD-grown $\text{MoO}_{x,\text{C}_y}$ electrocatalysts, synchrotron-radiation-based X-ray absorption fine structure (XAFS) measurements were conducted. As shown in Fig. 3c, the normalized X-ray absorption near-edge structure (XANES) at the Mo K-edge revealed that the pre-edges of both HP-MoOC and HCP-MoOC were located between those of Mo foil and commercial MoO_2 powder. This finding suggested that the average valence state of Mo atoms in HP-MoOC and HCP-MoOC ranged from 0 to +4, indicating an increased electron density around the Mo atoms due to the existence of Mo-C bonding in $\text{MoO}_{x,\text{C}_y}$. Furthermore, the pre-edge of HCP-MoOC shifted to a lower energy compared to that of HP-MoOC, suggesting a more reduced valence state of Mo in HCP-MoOC. This observation is consistent with the XPS results, confirming the higher degree of carbon integration into the HCP-MoOC lattice structure. The local environment of Mo atoms was further analyzed through the k^2 -weighted Fourier-transformed extended X-ray absorption fine structure (FT-EXAFS) in R -space (Fig. 3d). The intensity of the Mo-O bond peak decreased progressively from MoO_2 to HP-MoOC to

HCP-MoOC, while the Mo-C bond peak became prominent in HCP-MoOC. This trend indicated that carbon atoms were initially introduced into the MoO_2 lattice during the first-step HP growth, with further carbon incorporation occurring during the second-step CH_4 plasma treatment. These spectroscopic results suggested that carbon incorporation led to a redistribution of local electronic density, enhancing the electron-rich character of Mo while altering the polarity of Mo-O bonds, which was beneficial for stabilizing Mo in $\text{MoO}_{x,\text{C}_y}$ catalyst materials and weakening the binding strength of Mo-H, thereby enhancing the HER activity^{52,53}.

HER activity evaluation

HER electrocatalytic activities of the plasma-grown catalysts were evaluated using a three-electrode electrochemical configuration in a 0.5 M H_2SO_4 electrolyte. Figure 4a shows that the plasma-grown $\text{MoO}_{x,\text{C}_y}$ catalysts significantly outperform the commercial MoO_2 powder catalyst, and HCP-MoOC shows better electrocatalytic performance than HP-MoOC. Notably, the overpotentials (η) of both HP-MoOC and HCP-MoOC catalysts are competitive with those of the most widely used commercial noble metal Pt/C catalyst at large current densities ($j > 1 \text{ A cm}^{-2}$). Specifically, the η values for HCP-MoOC at current densities of 5 A cm^{-2} and 10 A cm^{-2} are $358 \pm 2 \text{ mV}$ and $415 \pm 2 \text{ mV}$, respectively, which are lower than those of the existing advanced acidic HER catalysts^{54–57}, as shown in Fig. S13 and Supplementary Table S1. HCP-MoOC also demonstrates the capability to sustain even higher current densities, highlighting its high intrinsic activity and potential for high-rate hydrogen production (Fig. S14). The relationship between current density and the ratio of overpotential change to logarithmic current density change ($\Delta\eta/\Delta\log j|$) is analyzed for different catalysts and shown in Fig. 4b. This metric, a critical indicator of the electrocatalysts' energy efficiency performance at high current densities, is essential for practical hydrogen evolution applications^{58,59}. While the $\Delta\eta/\Delta\log j|$ ratio of the Pt/C catalyst increased sharply with current density, those of HP-MoOC and HCP-MoOC maintained lower values, suggesting their better performance at higher current densities. Notably, HCP-MoOC exhibited smaller $\Delta\eta/\Delta\log j|$ ratios compared to HP-MoOC at all current densities, indicating the higher electrocatalytic performance of HCP-MoOC. Moreover, a segmented Tafel slope analysis was conducted to further analyze the HER kinetics. In the low current density regions of 1 – 10 and 10 – 50 mA cm^{-2} , HCP-MoOC exhibited Tafel slopes of approximately 40.8 and 51.0 mV dec^{-1} , respectively, which suggested a Volmer-Heyrovsky mechanism, indicating that electrochemical desorption (i.e., Heyrovsky step) is the primary rate-limiting step^{60,61}. At current densities above 200 mA cm^{-2} , the Tafel slopes increased sharply above 100 mV dec^{-1} , likely due to mass transport limitations caused by proton depletion, which obscures the intrinsic kinetics⁶².

The HER performance of the HCP-MoOC catalysts at high current densities can be attributed to three factors: (i) Localized electric field effect. As reported in our previous work⁶³, the presence of ultrasharp edges generates a strong localized electric field, effectively driving H_3O^+ ion diffusion toward the reactive surface. This effect can be further analyzed by electrochemical impedance spectroscopy (EIS). As shown in the Nyquist plots (Fig. 4c), the charge transfer resistance (R_{ct}), represented by the diameter of the semicircles, decreases significantly as the applied potential increases, which is characteristic of enhanced reaction kinetics under higher overpotentials, as observed in other HER catalysts⁶⁴, where increased driving force lowers the kinetic barrier for charge transfer. In the case of HCP-MoOC, beyond the kinetic acceleration at higher applied potentials, we hypothesize that the nanoedge-enriched morphology further enhances the local electric field at the catalyst surface^{63,65}, which can promote more favorable hydrogen adsorption and facilitate interfacial electron transfer. Consequently, the rapid consumption of H_3O^+ at high current densities can

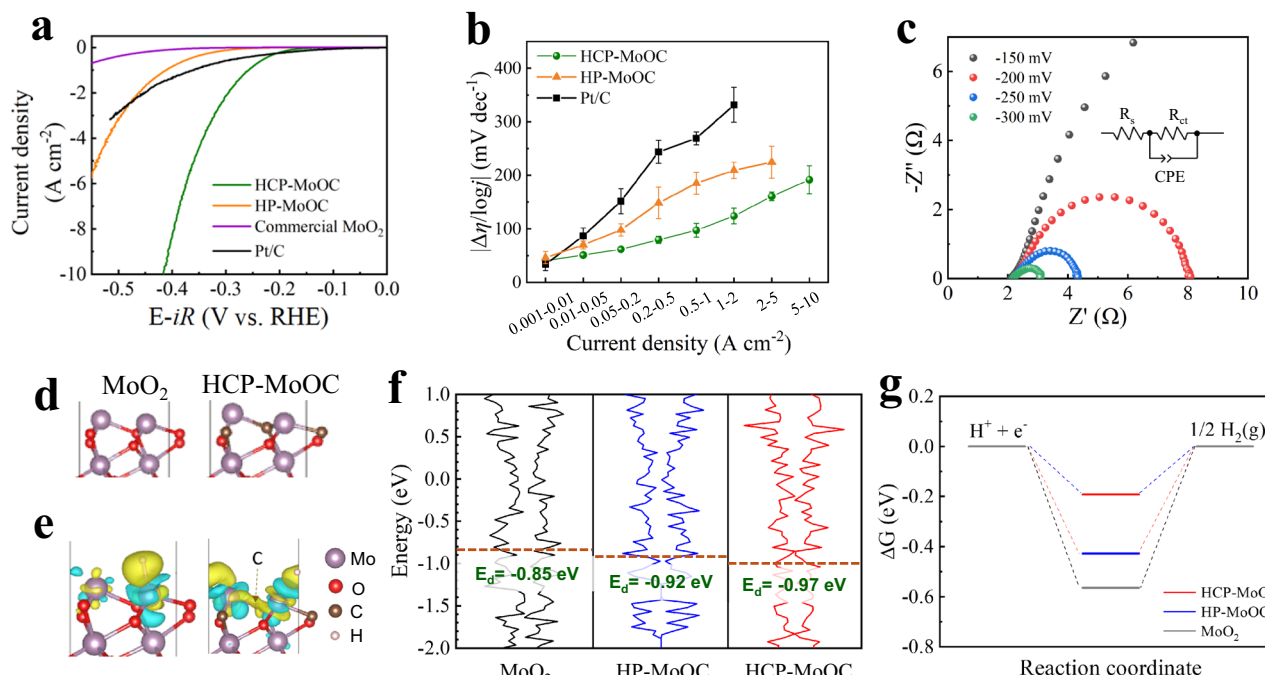


Fig. 4 | Electrochemical performance and characterization of MoO_xCy electrocatalysts and the underlying mechanism. **a** Polarization curves of HCP-MoOC, HP-MoOC, and commercial Pt/C and MoO_2 catalysts. The polarization curves without $i\text{R}$ compensation are shown in Fig. S15. All tests were conducted at room temperature (23 °C). **b** $|\Delta\eta/\Delta\log(j)|$ ratios for Pt/C, HP-MoOC, and HCP-MoOC in different current density ranges. The error bars correspond to the standard deviation calculated from three separate experimental replicates. **c** Nyquist plots

for HCP-MoOC at different potentials vs RHE, demonstrating the relationship between charge transfer resistance and applied potential. **d** Atomic models and **e** charge distributions of MoO_2 and HCP-MoOC catalysts. **f** Projected density of states (PDOS) of MoO_2 , HP-MoOC, and HCP-MoOC catalysts. Dashed lines indicate the d -band centers of Mo. **g** DFT-calculated Gibbs free energy (ΔG_H) variations for HER on MoO_2 , HP-MoOC, and HCP-MoOC catalysts.

be compensated, ensuring sustained high HER efficiency. (ii) Efficient H_2 bubble release. One of the major challenges for HER catalysts under industrial conditions is the formation of gas bubbles, which can obstruct active sites and limit reaction efficiency⁶⁶. The vertically standing petal-like morphology of HCP-MoOC reduces the interfacial adhesion to hydrogen bubbles, enabling the rapid detachment of generated H_2 at high current densities, attributed to the increased surface roughness. As shown in Supplementary Fig. S16, hydrogen bubbles generated on the Pt/C surface exhibited strong adhesion and grew to significant sizes, effectively covering many active sites and consequently hindering subsequent catalytic reactions. In contrast, smaller hydrogen bubbles formed on the HCP-MoOC surface were readily detached from the catalyst, ensuring continuous exposure of active sites to the electrolyte and enabling sustained HER activity at high current densities. (iii) Weakened hydrogen adsorption free energy (ΔG_H), stemming from carbon incorporation into lattices of MoO_2 . In addition, the reducing plasma environment (i.e., H_2 and CH_4) is expected to induce oxygen vacancies^{67,68}, which could synergistically enhance the electrical conductivity and electrocatalytic HER performance⁶⁹. To quantitatively determine the atomic ratio within the crystalline structure of HCP-MoOC, we further conducted HP treatment to etch the surface carbon layer (details in Supplementary Note S1). After etching, the HCP-MoOC showed a slight increase in HER activity but significantly reduced stability (Supplementary Fig. S17), indicating that the surface carbon layer played a critical role in achieving good stability of HCP-MoOC. Such a phenomenon has also been observed in previously reported carbon-encapsulated catalysts^{70,71}. EDX analysis on the etched HCP-MoOC revealed that the Mo:O:C atomic ratio in the crystalline part of HCP-MoOC was approximately 1:1:1 (Supplementary Fig. S18), confirming a higher carbon content than that in HP-MoOC.

The electrocatalytic performance of HCP-MoOC was further supported by density functional theory (DFT) calculations. As shown in Fig. 4d and Supplementary Fig. S19a, atomic models for various catalysts, including MoO_2 and MoO_xCy with different Mo:O:C ratios (1:1.5:0.5 for HP-MoOC and 1:1:1 for HCP-MoOC), were constructed to simulate different Mo-based phases formed under different plasma treatment conditions. Figure 4e presents the electron charge distribution after H adsorption on MoO_2 and HCP-MoOC. In the case of MoO_2 , the electron transfers predominantly occurred from H to Mo, leading to a strong interaction between the two elements. However, for HCP-MoOC, electron transfer from C to Mo also exists, alongside the electron transfer from H. This suggests that the presence of carbon in HCP-MoOC reduces the interaction between hydrogen and molybdenum, thereby weakening the bond strength between them. Additionally, the d -band center of molybdenum in HCP-MoOC is lower than those in MoO_2 and HP-MoOC, indicating that molybdenum is more stabilized by carbon substitution in HCP-MoOC than in MoO_2 or HP-MoOC. The d -band center refers to the weighted average energy level of the d -electrons in a transition metal and serves as a widely used descriptor for catalytic activity and bonding strength with adsorbates such as hydrogen. A lower d -band center typically corresponds to weaker metal–hydrogen interactions, favoring easier hydrogen desorption. This electronic stabilization induced by carbon insertion plays a crucial role in optimizing hydrogen adsorption energy, thereby improving the intrinsic catalytic activity of the material (Fig. 4f). The calculated oxidation state of Mo in HCP-MoOC (1.61) was also lower than that in MoO_2 (1.66), which corresponded well with the experimental Mo K-edge XANES spectra. This stabilization of Mo in HCP-MoOC due to C substitution led to a weakened Mo–H bonding strength, enhancing the HER performance of HCP-MoOC. As illustrated in Fig. 4g, HCP-MoOC exhibited the most favorable ΔG_H (i.e.,

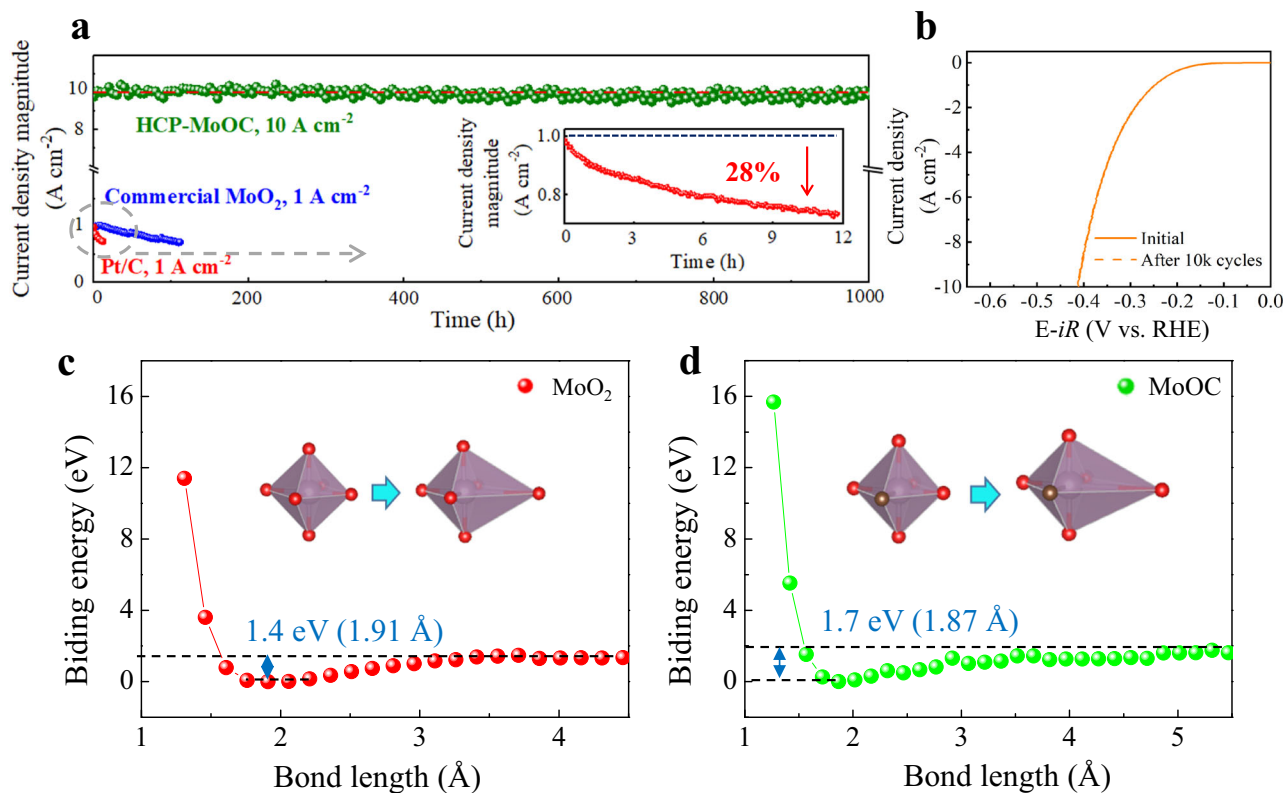


Fig. 5 | Durability performance of MoO_xC_y and the underlying mechanism.
a Chronoamperometric tests of HCP-MoOC, commercial Pt/C, and MoO₂ catalysts. The

resistivity of the catalyst ($2.50 \pm 0.02 \Omega$) remained stable throughout the cycling. Calculated Mo-O binding energy and bond length of **c** MoO₂ and **d** HCP-MoOC.

closest to 0 eV) among the catalysts, indicating its optimal binding with hydrogen atoms and thus exhibiting competitive HER activity compared to other catalysts.

Long-term HER performance

Achieving high-performance hydrogen production requires overcoming several challenges, such as OER efficiency and membrane degradation⁷². However, enhancing HER catalyst stability under industrial-level current densities in acidic media presents a valuable opportunity for advancing practical hydrogen technologies⁷³. Given that hydrogen production throughput, which depends on both the operating current density and the catalyst lifetime, is a critical metric for industrial applications, the development of robust, high-efficiency HER catalysts is essential for scalable and sustainable hydrogen production. This parameter directly influences the efficiency, stability, cost per liter of produced hydrogen (see note S3 for cost estimation), and scalability of hydrogen production in practice. The grown HCP-MoOC exhibited a high hydrogen production throughput of up to 4477.4 L cm⁻² at a high generation rate, surpassing the DOE target (>1253.7 L cm⁻²) and demonstrating strong competitiveness with state-of-the-art HER catalysts^{54,56,57,59,74-80} (Fig. S20 and Supplementary Table S2). The notable H₂ throughput of the HCP-MoOC is derived from the stable operation of the electrocatalyst over 1000 h at high current densities. To demonstrate the stability of the HCP-MoOC catalyst, chronoamperometric (*j*-*t*) tests were conducted at a high current density of 10 A cm⁻² with the applied potential fixed at -415 mV vs RHE (Fig. 5a). The HCP-MoOC catalyst exhibited stable operation in 0.5 M H₂SO₄ during the tests, with negligible degradation (i.e., approx. 0.11%) over 1000 h. This performance exceeded the target (i.e., >3 A cm⁻² for 1000 h with 0.13% degradation) proposed by the U.S. DOE⁸. Notably, the catalyst exhibited no performance degradation at 10 A cm⁻² even

after 1000 h of continuous operation (Fig. S21). At ultrahigh current densities (>1 A cm⁻²), transient performance fluctuations may be observed due to vigorous gas evolution, which can momentarily block active sites. Normal catalytic activity resumes upon bubble detachment. Future improvements in electrode architecture, advanced cell configuration design, and optimized gas release pathways may further mitigate such effects. Post-stability analysis revealed no significant changes in the microstructure or crystal structure, and the sharp nanoedges of the vertically aligned nanosheets remained intact (Figs. S22 and S23). In contrast, the commercial Pt/C catalysts displayed severe degradation during the chronoamperometry tests, with the performance decreased by 28% in 12 h, even at a much lower current density of approx. 1 A cm⁻², a phenomenon that has also been reported in previous studies^{81,82}. We note that the chronoamperometric test of the Pt/C catalyst was conducted at 1 A cm⁻² instead of 10 A cm⁻², because the Pt/C catalyst deteriorated rapidly at such an ultrahigh current density. Substantial performance degradation was also observed during the repeated linear sweep voltammetry tests at such ultrahigh current densities (Supplementary Fig. S24). The calculated expected lifetime of the HCP-MoOC catalyst, based on the 10% performance degradation threshold defined by the DOE, is approximately 90,909 h, which exceeds the DOE's ultimate target (80,000 h) and demonstrates long-term durability greater than that of state-of-the-art HER catalysts reported to date (Supplementary Fig. S25 and Table S2). Notably, the hydrogen lifetime throughput of HCP-MoOC (~407,033.6 L cm⁻²) overpassed the DOE target (100,503.1 L cm⁻²), demonstrating the great potential for large-scale applications.

Moreover, the polarization curve of HCP-MoOC showed a negligible shift after 10,000 cyclic voltammetry (CV) cycles (Fig. 5b), indicating stable performance under acidic HER conditions. To further understand the notable stability of HCP-MoOC, the binding energies

between the metal atom and adjacent atoms in the Mo-based catalysts were calculated, as shown in Fig. 5c, d. This analysis is crucial to assessing the lattice stability of catalysts, which plays a vital role in combating electrochemical decomposition and maintaining long-term HER performance at high current densities. Fig. 5c, d illustrate that carbon incorporation into the MoO_2 lattice increases the binding energy from 1.4 to 1.7 eV, contributing to the enhanced structural stability of the HCP-MoOC catalyst under demanding electrochemical conditions. It is inferred that this stronger atomic interaction helps preserve the crystalline framework of the catalyst during prolonged high-current operation, thereby minimizing long-term degradation. Furthermore, the Mo-O bonding lengths of MoO_2 and HCP-MoOC at equilibrium states are calculated to be 1.91 Å and 1.87 Å, respectively (Fig. 5c, d), indicating that the bond length decreases as the binding energy increases. This shortened bond length suggests that the lattice would be contracted in MoOC, as evidenced by the shift of its XRD peak toward a higher angle.

In summary, we report the design and realization of an efficient and stable catalyst based on molybdenum oxycarbide (i.e., MoO_xC_y) nanosheets with petal-like structures and controlled chemical compositions by PECVD using salts as solid precursors. The plasma-grown, nanoedge-enriched MoO_xC_y catalyst with a uniform phase exhibits efficient acidic HER performance with a low overpotential of 415 mV at a high current density of up to 10 A cm^{-2} for 1000 h (>41 days). As a result, a high H_2 throughput of $4,477.4 \text{ L cm}^{-2}$ and expected lifetime of 90,909 h are achieved, highlighting its competitiveness with state-of-the-art transition metal- and even noble metal-based catalysts in both throughput and stability. This work provides a pathway for developing catalysts suitable for practical industrial electrocatalytic acidic hydrogen evolution.

Methods

Chemicals and materials

Chemicals, including MoO_3 (99%), sodium chloride (99%), ethanol (200 proof), and sulfuric acid (98%), were purchased from Sigma-Aldrich. Other chemicals, including isopropyl alcohol (IPA, 98%) and acetone (>99.5%), were purchased from Thermo Fisher Scientific. Carbon cloth was purchased from Fuel Cell Earth. Silver paste was purchased from Ted Pella Inc. Graphite plates (99.99%) were purchased from CGjiogujio. Nafion 117 membrane was purchased from Ion Power Co.

Fabrication of HP-MoOCs

HP-MoOCs were synthesized by a customized inductively coupled plasma enhanced chemical vapor deposition (PECVD) system. In a typical procedure, carbon cloth was cut into $4 \text{ cm} \times 1 \text{ cm}$ pieces and sequentially washed with acetone, IPA, and water. Next, 20 g MoO_3 and 10 g NaCl were added to 100 mL of ethanol and stirred for 4 h. After drying overnight, the resulting salt precursors were collected for the PECVD growth of MoO_xC_y . 0.75 g salt precursor was placed in a crucible boat, with a piece of carbon cloth positioned 2 cm away from the precursor. The tube was then evacuated to a pressure of <3 Pa and heated to 600 °C. A hydrogen gas flow of 6 mL min^{-1} was introduced, and a 300 W radio frequency source was coupled into the quartz tube to initiate the growth of HP-MoOC on the carbon cloth substrate. The growth process was maintained at ~30 Pa for 20 min. Afterward, the sample was cooled under an argon flow of 20 mL min^{-1} to obtain HP-MoOC.

Fabrication of HCP-MoOCs

The fabrication of HCP-MoOC involved a second step of plasma treatment after the first-step growth of HP-MoOC. For the plasma treatment, temperature was increased from 600 to 650 °C, and CH_4 was introduced into the PECVD system at a flow rate of 6 mL min^{-1} . A 300 W radio frequency source was coupled into the quartz tube to

initiate methane plasma treatment. After 10 min of plasma treatment, the sample was cooled under an argon flow of 20 mL min^{-1} to obtain HCP-MoOC. To further investigate the tunability of carbon incorporation, additional samples were fabricated with CH_4 plasma treatment times of 3 and 5 min, while all other synthesis parameters were kept constant (see Section S3 and Supplementary Fig. S26).

Materials characterization

SEM (SUPRA40, Zeiss) was applied to characterize the morphology of the samples at an acceleration voltage of 10 kV. Transmission electron microscopy (TEM) and high-resolution TEM (HRTEM) were conducted on JEOL JEM-2100F (JEOL) at an acceleration voltage of 200 kV. STEM-EDX analysis was performed on Spectra 200 at 200 kV. X-ray photoelectron spectra (XPS) were collected with a Physical Electronics Versa Probe II system. Powder XRD spectra were recorded on Bruker D8 P-XRD operating at 40 kV and 40 mA with $\text{Cu K}\alpha$ radiation. The XAS characterizations were conducted at 7-BM in Brookhaven National Laboratory. All tests were conducted at a room temperature of ~23 °C and atmospheric pressure of ~0.1 MPa, with a humidity of ~49%. Error analysis was conducted with multiple sets of repeatable tests.

Electrochemical characterization

Electrochemical measurements were performed using a 1010E Electrochemical Workstation (Gamry) in a conventional three-electrode setup. A graphite rod was used as the counter electrode and a saturated calomel electrode (SCE) as the reference electrode, calibrated using Pt plates as the counter and working electrodes in H_2 -saturated 0.5 M H_2SO_4 . For stability tests, a graphite plate served as the counter electrode. The working electrodes were HP-MoOC or HCP-MoOC with an exposed area of 0.1 cm^2 . For the characterization of commercial Pt/C and MoO_2 powder samples, 2 mg of each catalyst was dispersed into 1.0 mL of absolute ethanol and 40 μL of Nafion solution (5.0 wt%) to form a homogeneous catalyst ink (2 mg mL^{-1}) via 1-h sonication. 250 μL of the ink was then dropped on the surface of a $1 \text{ cm} \times 1 \text{ cm}$ (~0.5 mg cm^{-2}) carbon cloth and dried overnight. A Nafion 117 membrane was cut into a circle ($d = 16 \text{ mm}$) and used to separate the cathodic and anodic compartments. The membrane was pretreated with 3 wt% H_2O_2 for 1 h, followed by DI water at 80 °C for 2 h. HER measurements were performed in 0.5 M H_2SO_4 solution ($\text{pH} = 0.3 \pm 0.1$), prepared by adding 103.24 g of concentrated H_2SO_4 to a 2-L flask, followed by the gradual addition of DI water with agitation for 1 h. After preparation, the electrolyte was stored in a sealed container at room temperature. The resistance (R_u) of the 0.5 M H_2SO_4 solution was measured to be $1.61 \pm 0.04 \Omega$.

Polarization curves were recorded at a scan rate of 2 mV s^{-1} with automatic iR compensation, and the accelerated durability tests were performed by applying the cyclic potential sweeps for 10,000 cycles. The dynamic resistivity of the catalysts was recorded by the potentiostat during the test. EIS measurements were conducted across various potentials within a frequency spectrum extending from 100 kHz to 100 mHz, utilizing an alternating current (AC) amplitude of 10 mV. All potentials were recorded against the SCE and calibrated with respect to a reversible hydrogen electrode (RHE):

$$E_{RHE} = E_{SCE} + 0.244 + 0.059 \times pH \quad (2)$$

DFT calculations

The atomic and electronic structures of MoO_2 , HP-MoOC ($\text{MoO}_{1.5}\text{C}_{0.5}$), and HCP-MoOC (MoOC) were modeled by DFT using the Vienna Ab Initio Simulation Package (VASP). The exchange-correlation function and the spin-polarized generalized gradient approximation were parameterized by Perdew-Burke-Ernzerhof (PBE)⁸³. A Monkhorst-Pack grid of $4 \times 4 \times 1$ K-points sampling and a cut-off energy of 500 eV were applied. The oxidation charge state was

calculated based on Bader charge analysis⁸⁴. The free energy of HER was analyzed based on the Volmer mechanism ($H^+ + e^- \rightarrow H^*$), where H^* represents the adsorbed hydrogen atom on the atomic models. The Gibbs free energy of H adsorption (ΔG_H) was analyzed according to⁸⁵:

$$\Delta G_{H^*} = \Delta E + \Delta E_{ZPE} - T\Delta S \quad (3)$$

where ΔE_{ZPE} is the zero-point energy (ZPE), T is the temperature, and ΔS is the entropy variation. Here, the adsorption energy of the hydrogen atom, ΔE , was calculated by:

$$\Delta E = E_{H\text{-model}} - E_{\text{model}} - \frac{1}{2}E_H \quad (4)$$

where $E_{H\text{-model}}$, E_{model} , and E_H are the total energy H-adsorbed model, the H-free model, and the hydrogen gas, respectively. In addition, the binding energies of MoO_2 and $MoOC$ were calculated by changing the Mo-O bond distance in octahedral structures:

$$\text{Binding energy} = E_{\text{Stable_Mo-O}} - E_{\text{Var_Mo-O}} \quad (5)$$

where $E_{\text{Stable_Mo-O}}$ and $E_{\text{Var_Mo-O}}$ are the total energy of the most stable state and the total energy depending on variations of bond length, respectively. The relaxed atomic models (.cif format) are provided in the Supplementary Data file 1. doc file.

Data availability

All relevant data that support the findings of this study are presented in the manuscript and supplementary information file. Source data are provided with this paper.

References

- Wang, Z.-J. et al. Low-iridium-content IrNiTa metallic glass films as intrinsically active catalysts for hydrogen evolution reaction. *Adv. Mater.* **32**, 1906384 (2020).
- Cheng, L. et al. Ultrathin WS₂ nanoflakes as a high-performance electrocatalyst for the hydrogen evolution reaction. *Angew. Chem. Int. Ed.* **53**, 7860–7863 (2014).
- Zhu, Y. et al. Metal oxide-based materials as an emerging family of hydrogen evolution electrocatalysts. *Energy Environ. Sci.* **13**, 3361–3392 (2020).
- Wang, K. et al. Dense platinum/nickel oxide heterointerfaces with abundant oxygen vacancies enable ampere-level current density ultrastable hydrogen evolution in alkaline. *Adv. Funct. Mater.* **33**, 2211273 (2023).
- Tsounis, C. et al. Pt single atom electrocatalysts at graphene edges for efficient alkaline hydrogen evolution. *Adv. Funct. Mater.* **32**, 2203067 (2022).
- Jin, M. et al. Strategies for designing high-performance hydrogen evolution reaction electrocatalysts at large current densities above 1000 mA Cm⁻². *ACS Nano* **16**, 11577–11597 (2022).
- Guo, F. et al. Recent advances in ultralow-pt-loading electrocatalysts for the efficient hydrogen evolution. *Adv. Sci.* **10**, 2301098 (2023).
- Open Energy Data. Energy. gov. <https://www.energy.gov/eere/fuelcells/technical-targets-proton-exchange-membrane-electrolysis> (accessed 2024-05-07).
- Wang, H. et al. Super-hybrid transition metal sulfide nanoarrays of Co_3S_4 nanosheet/P-doped WS₂ nanosheet/Co₉S₈ nanoparticle with Pt-like activities for robust all-pH hydrogen evolution. *Adv. Funct. Mater.* **32**, 2112362 (2022).
- Xiong, W., Yin, H., Wu, T. & Li, H. Challenges and opportunities of transition metal oxides as electrocatalysts. *Chem. A Eur. J.* **29**, e202202872 (2023).
- Al-Naggar, A. H., Shinde, N. M., Kim, J.-S. & Mane, R. S. Water splitting performance of metal and non-metal-doped transition metal oxide electrocatalysts. *Coord. Chem. Rev.* **474**, 214864 (2023).
- Sher Shah, M.d.S. A., Jang, G. Y., Zhang, K. & Park, J. H. Transition metal carbide-based nanostructures for electrochemical hydrogen and oxygen evolution reactions. *EcoEnergy* **1**, 344–374 (2023).
- Oh, Y. et al. Pulsed laser interference patterning of transition-metal carbides for stable alkaline water electrolysis kinetics. *Carbon Energy* **6**, e448 (2024).
- Houston, J. E., Laramore, G. E. & Park, R. L. Surface electronic properties of tungsten, tungsten carbide, and platinum. *Science* **185**, 258–260 (1974).
- Yang, C. et al. Structural transformation of molybdenum carbide with extensive active centers for superior hydrogen evolution. *Nano Energy* **98**, 107232 (2022).
- Gómez-Marín, A. M. & Ticianelli, E. A. Effect of transition metals in the hydrogen evolution electrocatalytic activity of molybdenum carbide. *Appl. Catal. B Environ.* **209**, 600–610 (2017).
- Zu, M. Y. et al. Bimetallic carbide as a stable hydrogen evolution catalyst in harsh acidic water. *ACS Energy Lett.* **3**, 78–84 (2018).
- Wang, S. et al. Synergistic improvement of pH-universal hydrogen evolution through B, N dual-doped Mo₂C. *J. Mater. Chem. A* **13**, 3084–3093 (2025).
- Wang, B. et al. Surface excited MoO₂ to master full water splitting. *Electrochim. Acta* **359**, 136929 (2020).
- Hayami, W., Tang, S., Chiu, T.-W. & Tang, J. Reduction in work functions of transition-metal carbides and oxycarbides upon oxidation. *ACS Omega* **6**, 14559–14565 (2021).
- Zhang, L., Zhao, X., Yuan, Z., Wu, M. & Zhou, H. Oxygen defect-stabilized heterogeneous single atom catalysts: preparation, properties and catalytic application. *J. Mater. Chem. A* **9**, 3855–3879 (2021).
- Wasan Awin, E. et al. Novel precursor-derived meso-/macroporous TiO₂/SiOC nanocomposites with highly stable anatase nanophase providing visible light photocatalytic activity and superior adsorption of organic dyes. *Materials* **11**, 362 (2018).
- Chen, K. et al. Strengthened d-p Orbital Hybridization on Meta-stable Cubic Mo₂C for Highly Stable Lithium-Sulfur Batteries. *ACS Nano* **18**, 34791–34802 (2024).
- Wang, Z. et al. Manipulation on active electronic states of meta-stable phase β -NiMoO₄ for large current density hydrogen evolution. *Nat. Commun.* **12**, 5960 (2021).
- Sun, X. et al. Reaction-induced unsaturated mo oxycarbides afford highly active CO₂ conversion catalysts. *Nat. Chem.* **16**, 2044–2053 (2024).
- Kurlov, A. et al. Exploiting two-dimensional morphology of molybdenum oxycarbide to enable efficient catalytic dry reforming of methane. *Nat. Commun.* **11**, 4920 (2020).
- Kumar, A. & Bhan, A. Oxygen content as a variable to control product selectivity in hydrodeoxygenation reactions on molybdenum carbide catalysts. *Chem. Eng. Sci.* **197**, 371–378 (2019).
- Witvrouw, T., Paulussen, S. & Sels, B. The use of non-equilibrium plasmas for the synthesis of heterogeneous catalysts. *Plasma Process. Polym.* **9**, 750–760 (2012).
- Neyts, E. C., Ostrikov, K. K., Sunkara, M. K. & Bogaerts, A. Plasma catalysis: synergistic effects at the nanoscale. *Chem. Rev.* **115**, 13408–13446 (2015).
- Wang, Z. et al. Catalyst preparation with plasmas: how does it work? *ACS Catal.* **8**, 2093–2110 (2018).
- Liang, T. et al. Ultra-fast non-equilibrium synthesis and phase segregation in $In_xSn_{1-x}Te$ thermoelectrics by SHS-PAS processing. *J. Mater. Chem. C* **3**, 8550–8558 (2015).
- Taccogna, F. & Dilecce, G. Non-equilibrium in low-temperature plasmas. *Eur. Phys. J. D* **70**, 251 (2016).

33. Tanaka, I., Okubo, H. & Harada, Y. Diamond synthesis on Si by plasma chemical vapor deposition using microwave sheath-voltage combination plasma. *Surf. Coat. Technol.* **423**, 127592 (2021).

34. Tang, C. C. & Hess, D. W. Plasma-enhanced chemical vapor deposition of β -tungsten, a metastable phase. *Appl. Phys. Lett.* **45**, 633–635 (1984).

35. Tamayo, A., Mazo, M. A., Rubio, F. & Rubio, J. Structure properties relationship in silicon oxycarbide glasses obtained by spark plasma sintering. *Ceram. Int.* **40**, 11351–11358 (2014).

36. Franz, G. Plasma enhanced chemical vapor deposition of organic polymers. *Processes* **9**, 980 (2021).

37. Zhou, J. et al. A library of atomically thin metal chalcogenides. *Nature* **556**, 355–359 (2018).

38. Li, S. et al. Mixed-salt enhanced chemical vapor deposition of two-dimensional transition metal dichalcogenides. *Chem. Mater.* **33**, 7301–7308 (2021).

39. Tang, L., Tan, J., Nong, H., Liu, B. & Cheng, H.-M. Chemical vapor deposition growth of two-dimensional compound materials: controllability, material quality, and growth mechanism. *Acc. Mater. Res.* **2**, 36–47 (2021).

40. Han, Z. J., Murdock, A. T., Seo, D. H. & Bendavid, A. Recent progress in plasma-assisted synthesis and modification of 2D materials. *2D Mater.* **5**, 032002 (2018).

41. Wu, S. et al. Molecular understanding of the effect of hydrogen on graphene growth by plasma-enhanced chemical vapor deposition. *Phys. Chem. Chem. Phys.* **24**, 10297–10304 (2022).

42. Zhang, H., Cao, T. & Cheng, Y. Preparation of few-layer graphene nanosheets by radio-frequency induction thermal plasma. *Carbon* **86**, 38–45 (2015).

43. Li, S. Salt-assisted chemical vapor deposition of two-dimensional transition metal dichalcogenides. *iScience* **24**, 103229 (2021).

44. Yang, X. et al. Feasibility of molecular dynamics simulation for process parameter guidance of silicon nitride thin films by PECVD. *Appl. Surf. Sci.* **654**, 159401 (2024).

45. Vallée, C. et al. Plasma deposition—impact of ions in plasma enhanced chemical vapor deposition, plasma enhanced atomic layer deposition, and applications to area selective deposition. *J. Vac. Sci. Technol. A Vac. Surf. Films* **38**, 033007 (2020).

46. Ferrari, A. C. & Basko, D. M. Raman spectroscopy as a versatile tool for studying the properties of graphene. *Nat. Nanotech* **8**, 235–246 (2013).

47. Zhang, Q. et al. A metallic molybdenum dioxide with high stability for surface enhanced raman spectroscopy. *Nat. Commun.* **8**, 14903 (2017).

48. Wu, X. et al. Solvent-free microwave synthesis of ultra-small Ru-Mo2C@CNT with strong metal-support interaction for industrial hydrogen evolution. *Nat. Commun.* **12**, 4018 (2021).

49. Pinder, J. W. et al. Avoiding common errors in X-ray photoelectron spectroscopy data collection and analysis, and properly reporting instrument parameters. *Appl. Surf. Sci. Adv.* **19**, 100534 (2024).

50. Liu, Y., Huang, B. & Xie, Z. Hydrothermal synthesis of core-shell MoO₂/ α -Mo2C heterojunction as high performance electrocatalyst for hydrogen evolution reaction. *Appl. Surf. Sci.* **427**, 693–701 (2018).

51. Yang, H. et al. Highly efficient electrocatalytic hydrogen evolution promoted by O-Mo-C interfaces of ultrafine β -Mo₂C nanosstructures. *Chem. Sci.* **11**, 3523–3530 (2020).

52. Jia, J. et al. Ultrathin N-doped Mo2C nanosheets with exposed active sites as efficient electrocatalyst for hydrogen evolution reactions. *ACS Nano* **11**, 12509–12518 (2017).

53. Yang, Y. et al. Water induced ultrathin Mo2C nanosheets with high-density grain boundaries for enhanced hydrogen evolution. *Nat. Commun.* **13**, 7225 (2022).

54. Yang, J. et al. Ultrahigh-current-density niobium disulfide catalysts for hydrogen evolution. *Nat. Mater.* **18**, 1309–1314 (2019).

55. Cheng, X. et al. Highly active, stable oxidized platinum clusters as electrocatalysts for the hydrogen evolution reaction. *Energy Environ. Sci.* **10**, 2450–2458 (2017).

56. Wu, J. et al. Scalable synthesis of 2D Mo2C and thickness-dependent hydrogen evolution on its basal plane and edges. *Adv. Mater.* **35**, 2209954 (2023).

57. Yu, Q. et al. A Ta-TaS₂ monolith catalyst with robust and metallic interface for superior hydrogen evolution. *Nat. Commun.* **12**, 6051 (2021).

58. Yang, L. et al. Glue-assisted grinding exfoliation of large-size 2D materials for insulating thermal conduction and large-current-density hydrogen evolution. *Mater. Today* **51**, 145–154 (2021).

59. Luo, Y. et al. Morphology and surface chemistry engineering toward ph-universal catalysts for hydrogen evolution at high current density. *Nat. Commun.* **10**, 269 (2019).

60. Kou, T. et al. Carbon doping switching on the hydrogen adsorption activity of nio for hydrogen evolution reaction. *Nat. Commun.* **11**, 590 (2020).

61. Shinagawa, T., Garcia-Esparza, A. T. & Takanabe, K. Insight on tafel slopes from a microkinetic analysis of aqueous electrocatalysis for energy conversion. *Sci. Rep.* **5**, 13801 (2015).

62. Xie, D. et al. High mass transfer rate in electrocatalytic hydrogen evolution achieved with efficient quasi-gas phase system. *Angew. Chem. Int Ed.* **64**, e202414493 (2025).

63. Xiong, G. et al. Bioinspired leaves-on-branchlet hybrid carbon nanostructure for supercapacitors. *Nat. Commun.* **9**, 790 (2018).

64. Kitajima, D., Misumi, R., Kuroda, Y. & Mitsushima, S. Relationship between bubble generation behavior and hydrogen evolution reaction performance at high current densities during alkaline water electrolysis. *Electrochim. Acta* **502**, 144772 (2024).

65. Yang, H. et al. Edge effects in vertically-oriented graphene based electric double-layer capacitors. *J. Power Sources* **324**, 309–316 (2016).

66. Luo, Y., Zhang, Z., Chhowalla, M. & Liu, B. Recent advances in design of electrocatalysts for high-current-density water splitting. *Adv. Mater.* **34**, 2108133 (2022).

67. Han, H. et al. Plasma-induced oxygen vacancies in amorphous mno_x boost catalytic performance for electrochemical CO₂ reduction. *Nano Energy* **79**, 105492 (2021).

68. Wang, K. et al. Plasma-induced oxygen defect engineering in perovskite oxide for boosting oxygen evolution reaction. *Small* **20**, 2404239 (2024).

69. Lu, J., Qian, G., Luo, L., He, H. & Yin, S. Contributions of oxygen vacancies to the hydrogen evolution catalytic activity of tungsten oxides. *Int. J. Hydrol. Energy* **46**, 676–682 (2021).

70. Deng, J. et al. Highly active and durable non-precious-metal catalysts encapsulated in carbon nanotubes for hydrogen evolution reaction. *Energy Environ. Sci.* **7**, 1919–1923 (2014).

71. Pi, C. et al. In situ formation of N-doped carbon-coated porous MoP nanowires: a highly efficient electrocatalyst for hydrogen evolution reaction in a wide pH range. *Appl. Catal. B Environ.* **263**, 118358 (2020).

72. Du, L., Sun, Y. & You, B. Hybrid water electrolysis: replacing oxygen evolution reaction for energy-efficient hydrogen production and beyond. *Mater. Rep. Energy* **1**, 100004 (2021).

73. Qiao, Z. et al. Cathode and anode catalysis mechanism and design principle of water all splitting in chlorinated neutral environment: a review. *Int. J. Hydrol. Energy* **63**, 1182–1196 (2024).

74. Zheng, Z. et al. Boosting hydrogen evolution on MoS₂ via co-confining selenium in surface and cobalt in inner layer. *Nat. Commun.* **11**, 3315 (2020).

75. Li, G. et al. Cobalt–cobalt phosphide nanoparticles@nitrogen–phosphorus doped carbon/graphene derived from cobalt ions adsorbed *Saccharomyces* yeasts as an efficient, stable, and large-

current-density electrode for hydrogen evolution reactions. *Adv. Funct. Mater.* **28**, 1801332 (2018).

76. Liu, R. et al. Design of aligned porous carbon films with single-atom Co–N–C sites for high-current-density hydrogen generation. *Adv. Mater.* **33**, 2103533 (2021).

77. Zhang, C. et al. High-throughput production of cheap mineral-based two-dimensional electrocatalysts for high-current-density hydrogen evolution. *Nat. Commun.* **11**, 3724 (2020).

78. Chen, Y. et al. Highly active, nonprecious electrocatalyst comprising borophene subunits for the hydrogen evolution reaction. *J. Am. Chem. Soc.* **139**, 12370–12373 (2017).

79. Sun, J. et al. Highly efficient hydrogen evolution from a mesoporous hybrid of nickel phosphide nanoparticles anchored on cobalt phosphosulfide/phosphide nanosheet arrays. *Small* **15**, 1804272 (2019).

80. Qiu, Y. et al. Synergistic effect between platinum single atoms and oxygen vacancy in MoO₂ boosting pH-universal hydrogen evolution reaction at large current density. *Chem. Eng. J.* **427**, 131309 (2022).

81. Wei, H. et al. Iced photochemical reduction to synthesize atomically dispersed metals by suppressing nanocrystal growth. *Nat. Commun.* **8**, 1490 (2017).

82. Cheng, N. et al. Platinum single-atom and cluster catalysis of the hydrogen evolution reaction. *Nat. Commun.* **7**, 13638 (2016).

83. Perdew, J. P., Burke, K. & Ernzerhof, M. Generalized gradient approximation made simple. *Phys. Rev. Lett.* **77**, 3865–3868 (1996).

84. Henkelman, G., Arnaldsson, A. & Jónsson, H. A fast and robust algorithm for bader decomposition of charge density. *Comput. Mater. Sci.* **36**, 354–360 (2006).

85. Nørskov, J. K. et al. Trends in the exchange current for hydrogen evolution. *J. Electrochem. Soc.* **152**, J23 (2005).

Acknowledgements

G.X. thanks the University of Texas at Dallas startup fund. G.X. and K.C. acknowledge the support from the BEACONS Center funded by the Department of Defense (DoD) and National Science Foundation (NSF) grant (No. 2324593). This research used resources 7-BM of the National Synchrotron Light Source II, a U.S. Department of Energy (DOE) Office of Science User Facility operated for the DOE Office of Science by Brookhaven National Laboratory under Contract No. DE-SC0012704. Work performed at the Center for Nanoscale Materials, a U.S. Department of Energy Office of Science User Facility, was supported by the U.S. DOE, Office of Basic Energy Sciences, under Contract No. DE-AC02-06CH11357. The authors thank Dr. Siyu Tian and Ruda Jian for their assistance in sample preparation.

Author contributions

S.W., T.H. and A.M. contributed equally to this manuscript. G.X., K.C., S.W., T.H. and A.M. conceived the idea. S.W. and A.M. contributed to the

experimental design, material synthesis, electrochemical measurements, data analysis, XRD and XPS characterization, and drafting of the initial manuscript. T.H. designed and performed the theoretical calculations and also contributed to writing the initial draft. T.L. and Y.L. assisted with TEM and XAS characterization and contributed to editing the draft. G.X., K.C. and D.H. provided overall supervision of the project and revised the manuscript. All authors discussed the results and commented on the manuscript.

Competing interests

The authors declare no competing interests.

Additional information

Supplementary information The online version contains supplementary material available at <https://doi.org/10.1038/s41467-025-65734-8>.

Correspondence and requests for materials should be addressed to Dewen Hou, Kyeongjae Cho or Guoping Xiong.

Peer review information *Nature Communications* thanks Menghao Yang, who co-reviewed with Mohamed Ait TamerdRoham Dorakhan, Liang Huang, and the other anonymous reviewer(s) for their contribution to the peer review of this work. A peer review file is available.

Reprints and permissions information is available at <http://www.nature.com/reprints>

Publisher's note Springer Nature remains neutral with regard to jurisdictional claims in published maps and institutional affiliations.

Open Access This article is licensed under a Creative Commons Attribution-NonCommercial-NoDerivatives 4.0 International License, which permits any non-commercial use, sharing, distribution and reproduction in any medium or format, as long as you give appropriate credit to the original author(s) and the source, provide a link to the Creative Commons licence, and indicate if you modified the licensed material. You do not have permission under this licence to share adapted material derived from this article or parts of it. The images or other third party material in this article are included in the article's Creative Commons licence, unless indicated otherwise in a credit line to the material. If material is not included in the article's Creative Commons licence and your intended use is not permitted by statutory regulation or exceeds the permitted use, you will need to obtain permission directly from the copyright holder. To view a copy of this licence, visit <http://creativecommons.org/licenses/by-nc-nd/4.0/>.

© The Author(s) 2025